Ricerche di Matematica
https://doi.org/10.1007/s11587-026-01056-1

Linear instability and nonlinear stability of thermal convection in porous medium with internal heat source and higher temperature gradient

Sanaa L. Khalaf[1] · **Akil J. Harfash**[1]

Received: 31 October 2025 / Accepted: 14 January 2026

Abstract

We study thermal convection in a porous layer governed by the Darcy-Brinkman model, incorporating internal heating and a higher-order thermal diffusion (bi-Laplacian) term that models hyper-diffusive heat transport. Linear normal-mode analysis and an energy method are used to determine, respectively, the instability threshold and a nonlinear stability bound across Brinkman coefficient, internal heating, and boundary-type parameters. For stability analysis, we employ complementary solvers for linear-onset convection and nonlinear energy stability, integrating the Moore-Penrose pseudoinverse with golden section search and eigenvalue tracking to determine critical Rayleigh numbers. To solve the eigenvalue systems resulting from stability analyses, two numerical methods are formulated: Method I uses conventional shifted Chebyshev polynomials, whereas the new method, Method II, employs boundary-satisfying trial functions that remove boundary rows and columns, reduce algebraic dimension, and improve conditioning. A residual-based audit measures the residuals of the equations and the boundary conditions across systematic variations in the number of trial functions, yielding a reliable accuracy-cost metric. The two numerical methods produce nearly identical eigenvalues and eigenfunctions and agree within numerical tolerance across all evaluations. The new method attains the required accuracy with fewer polynomials, typically about half as many as in Method I, thereby offering a clear advantage over the traditional approach. We expect that the suggested numerical method will have a big impact on future studies. Under stress-free and rigid-rigid velocity boundaries, increases in the Brinkman coefficient and the presence of rigid walls raise both stability margins, whereas stronger internal heating lowers the linear-onset and energy-stability thresholds.

✉ Akil Harfash
akilharfash@gmail.com

Sanaa Khalaf
sanaasanaa1978@yahoo.com

[1] Department of Mathematics, Faculty of Science, Basrah University, Basrah, Iraq

Published online: 09 February 2026

Keywords Chebyshev collocation · Darcy–Brinkman model · Energy stability · Higher-order diffusion · Internal heating · Linear instability · Porous-medium convection · Rayleigh number

Mathematics Subject Classification 76E06 · 76S05 · 35B35

1 Introduction

Thermal convection in porous media underpins many natural and engineered processes, including geothermal energy extraction [19], subsurface contaminant transport [47], chemical reactor design [35], and thermal insulation [27]. Temperature gradients generate buoyancy forces that drive flow through the interconnected pore space, thereby governing heat and mass transfer [37]. Foundational studies by Horton and Rogers [26] and by Lapwood [34] established the canonical Horton-Rogers-Lapwood (Darcy-Bénard) problem for a fluid-saturated, rigid, isotropic porous layer heated from below.

Within the standard mathematical framework, namely Darcy's law coupled with the energy equation under the Boussinesq approximation [43], a linear stability analysis leads to an eigenvalue problem that delineates stability boundaries in terms of key non-dimensional parameters, notably the Darcy-Rayleigh number, boundary conditions, and porosity. For impermeable, isothermal plates, the classical result is a critical Darcy-Rayleigh number $Ra_L = 4\pi^2$, reflecting the stabilising influence of matrix (Darcy) resistance [26, 34]. Because Ra_L is defined differently from the clear-fluid Rayleigh number, this threshold is not directly comparable with the classical Rayleigh-Bénard value for a pure fluid [12]. The threshold depends on the relative magnitudes of permeability and thermal diffusivity [37] and is further modified by pore-scale dispersion and effective thermal conductivity, which can enhance heat-transfer efficiency [28].

The Darcy model captures the main features of slow, viscosity-dominated flow, but it omits non-Darcy drag and viscous-shear effects that become important at higher permeabilities and near solid-fluid interfaces [6, 13, 16, 37]. The Brinkman extension adds a Laplacian term to the momentum balance, providing a continuous bridge between the Darcy and Stokes regimes and addressing these omissions [37, 43]. Rees showed that the Darcy-Brinkman formulation gives more accurate predictions of convective patterns in heterogeneous or composite porous media, especially when inertial effects are moderate [39].

Darcy's law is widely used for flow in porous media, but its validity is largely confined to low Reynolds numbers; accuracy degrades at higher velocities [6]. The Brinkman extension augments Darcy's momentum balance with a viscous-diffusion (Laplacian) term, bringing it closer to the Navier-Stokes description [7]. Analyses of Darcy-Brinkman convection in inclined layers show that finite Darcy numbers and shear layers modify the critical conditions for instability [40]. These developments are unified in the monograph of Nield and Bejan, which systematically compares the Darcy, Darcy-Forchheimer, and Darcy-Brinkman models across a broad parameter

range and identifies transitions between viscous, inertial, and shear dominated regimes [37].

Stability analysis is fundamental for real-world modelling because it determines whether small perturbations decay or grow, and thus underpins a model's reliability, safety, and predictive capability under realistic operating conditions [1, 15, 29]. In porous/bidisperse convection, Darcy-Forchheimer-Brinkman models can exhibit coincidence of the energy and linear thresholds, so linear theory gives the exact onset criterion [3, 4, 10, 22, 42]. Moreover, energy analyses for Brinkman flows with viscous dissipation show that apparently different dissipation prescriptions are equivalent in their implications for nonlinear stability [5, 20, 21, 23–25, 30, 44]. Building on this foundation, recent studies map linear and nonlinear correlations under diverse drivers [2]: rotation and anisotropy can yield either steady or overstable onset [11]; imposed throughflow provides a tunable control that shifts both linear and energy thresholds [9]; Korteweg-type capillarity yields complete stationary and oscillatory boundaries with rigorous energy bounds [45]; electrohydrodynamic forcing in nanofluid saturated anisotropic layers clarifies the roles of the Prandtl number, stress relaxation, electric Rayleigh number, and Brinkman-Darcy number at onset [14]; coupling uniform rotation with temperature dependent viscosity can induce oscillatory convection with closely aligned linear and nonlinear limits [10]; in nonisothermal Jeffreys fluids, strong vertical throughflow favours overstability and admits sufficient energy stability conditions [2]; and, with depth dependent internal heating in Brinkman bidisperse media, numerical variational analyses report a steady exchange of stabilities with quantitative proximity of linear and nonlinear thresholds [8].

Even though there has been a lot of research on convection in porous media, there is still no complete stability analysis in a full higher-gradient framework that looks at the effects of permeability, inertial (Forchheimer) drag, and viscous-shear (Brinkman) effects at the same time when heating from above [7, 16, 37, 43, 46]. The influence of bi-Laplacian terms on the temperature field, the onset of motion, and the subsequent nonlinear evolution is insufficiently delineated [45]. Using the Fried-Gurtin-Musesti theory, we create an incompressible model in which the momentum balance includes a velocity bi-Laplacian and, in line with recent developments, the energy balance includes a temperature bi-Laplacian. [17, 18, 36]. We determine the essential Rayleigh number and the associated wavenumber for the onset of convection resulting from vertical heating, explicitly accounting for spatial variability in the coefficients of the highest-order derivatives. [18, 45]. A thorough examination of linear instability and nonlinear energy stability clarifies how enhanced gradient effects modify stability thresholds and affect the resulting convective planform [41, 45].

The paper is organised as follows. Section 2 introduces the governing equations: the Darcy-Brinkman momentum balance coupled to a reaction-diffusion equation with Laplacian and bi-Laplacian terms. We also non-dimensionalise the system and state the stress-free and no-slip boundary conditions. Section 3 formulates the linear normal-mode instability problem and defines the eigenvalue condition for the critical thermal Rayleigh number, Ra_L. Section 4 develops the nonlinear energy-method framework, specifies the associated energy functional, and gives the threshold criterion for Ra_E. Section 5 details two Chebyshev collocation schemes: (i) the instability algorithm using the Moore-Penrose pseudoinverse, golden-section search, and eigenvalue track-

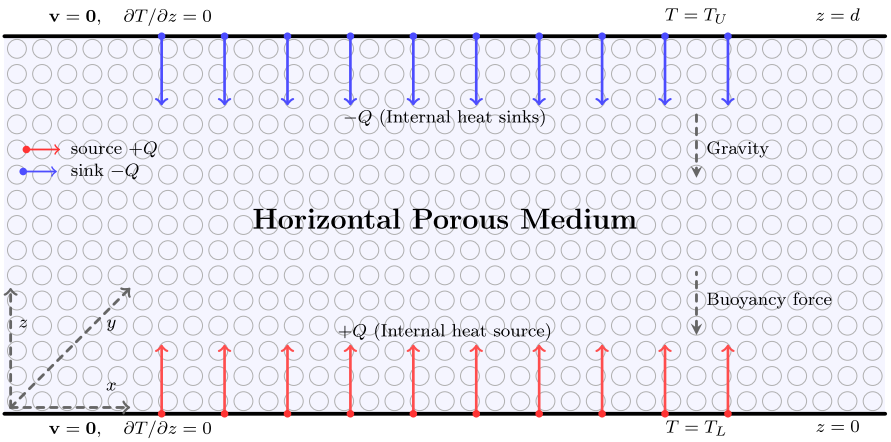

Fig. 1 Porous layer and thermal boundary conditions with an internal heat

ing; (ii) the stability algorithm for identifying Ra_E; and (iii) a residual-evaluation procedure that verifies accuracy and convergence. Section 6 reports a systematic parametric study of the principal dimensionless groups (the Brinkman coefficient, the hyper-diffusion parameter, and the internal heat-source magnitude) under both boundary conditions, and presents the resulting stability maps. Section 7 summarises the main findings, discusses their implications for engineered and natural porous systems, and outlines directions for future work.

2 Mathematical model: governing equations

Let us inspect a porous medium situated within the horizontal layer defined by $0 < z < d$. Consequently, we delineate our issue within the domain $\Psi = \{(x, y, z, t) \in \mathbb{R}^2 \times [0, d] \times \mathbb{R}^+\}$, representing all vectors in association with the standard Cartesian basis vectors $\mathbf{i}, \mathbf{j}, \mathbf{k}$. Let $\mathbf{v}$ represent the fluid velocity and T signify the temperature. The physical configuration, gravity direction, and thermal boundary conditions are illustrated in Fig. 1; the distributed internal heat source $+Q$ is depicted by upward red arrows with small circular tails. The model's governing equations are capable of being expressed as follows:

$$\begin{aligned} -\frac{\mu}{\kappa}\mathbf{v} - \nabla p - \mathbf{k}\rho_0 \mathrm{g}(1 - \varrho_T(T - T_0)) + \tilde{\chi}\,\Delta\mathbf{v} = 0, \\ \nabla \cdot \mathbf{v} = 0, \\ \frac{1}{M}\frac{\partial T}{\partial t} + \mathbf{v} \cdot \nabla T = \kappa_{t1}\Delta T - \kappa_{t2}\Delta^2 T + Q, \end{aligned} \tag{2.1}$$

where g denotes the gravitational acceleration, ρ_0 the reference density, κ the permeability, ϱ_T the thermal expansion coefficient, μ the dynamic viscosity, and κ_{t1} and κ_{t2} the thermal diffusivities. Moreover, p is the pressure, $\tilde{\chi}$ the Brinkman coefficient,

Table 1 Nomenclature

Symbol	Definition	Units
p	Pressure	Pa
T	Temperature	K
θ	Temperature perturbation	—
D	Differential operator $D \equiv \mathrm{d}/\mathrm{d}z$	—
a	Horizontal wavenumber (non-dimensional)	—
d	Layer depth (length scale)	m
κ	Permeability of porous matrix	m^2
μ	Dynamic viscosity	Pa s
ρ_0	Reference density	$\mathrm{kg\,m}^{-3}$
ϱ_T	Thermal expansion coefficient	$(\mathrm{mol\,m}^{-3})^{-1}$
κ_{t1}	Thermal diffusivity (Laplacian coefficient)	m^2/s
κ_{t2}	Hyper-diffusion (bi-Laplacian) coefficient	m^4/s
g	Gravitational acceleration	$\mathrm{m/s}^2$
β_T	Thermal expansion coefficient	K^{-1}
M	Heat-capacity ratio	—
Q	Constant internal heat source (or sink) in the heat equation	$\mathrm{K\,s}^{-1}$
λ	Brinkman drag parameter (inverse-Darcy)	—
$\hat{\kappa}$	Non-dimensional hyper-diffusion	—
q	Non-dimensional internal heating	—
Ra	Critical Rayleigh number (thermal)	—
Ra_L	Critical Rayleigh number (linear onset)	—
Ra_E	Critical Energy-stability threshold (nonlinear bound)	—

and M the ratio of the fluid's heat capacity to that of the porous medium. Finally, $\mathbf{k} = (0, 0, 1)$, Δ denotes the Laplacian operator, and Q is a constant internal heat source (or sink), whose inclusion permits the model to describe penetrative convection within the porous layer. To close the mathematical formulation of considered mathematical model, we prescribe on the following boundary conditions:

$$\begin{aligned} v_i &= 0, \qquad \text{at } z = 0 \text{ and } z = d, \\ T &= T_L, \quad \text{at } z = 0, \\ T &= T_U, \quad \text{at } z = d, \\ \frac{\partial T}{\partial z} &= 0, \qquad \text{at } z = 0 \text{ and } z = d, \end{aligned} \tag{2.2}$$

where T_L and T_U are the prescribed temperatures at the lower and upper boundaries, respectively, and $\beta_t = \frac{T_L - T_U}{d}$ is the constant temperature gradient imposed across the layer (See Table 1).

The stability of systems governed by partial differential equations arising in dynamical systems, fluid mechanics, and reaction-diffusion modelling rests on the behaviour

of a steady (equilibrium) state. To assess this, we linearise the nonlinear governing equations about the steady state and examine the evolution of small perturbations. If all perturbations decay, the equilibrium is stable; if any grow, it is unstable. Accordingly, we first determine the steady state $(\mathbf{u}, \bar{T}, \bar{p})$ by imposing $\mathbf{u} = 0$ and $\partial_t \bar{T} = 0$ in (2.1)-(2.2). This approach yields the following governing relations:

$$\bar{T}(z) = \beta_t \left(c_1 d\sqrt{\hat{\kappa}} \cosh\left(\frac{z}{d\sqrt{\hat{\kappa}}}\right) + c_2 d\sqrt{\hat{\kappa}} \sinh\left(\frac{z}{d\sqrt{\hat{\kappa}}}\right) + c_3 z + c_4 \right) - \frac{Q z^2}{2\kappa_{t1}}, \tag{2.3}$$

where

$$c_1 = \frac{2\sinh\left(\frac{1}{\sqrt{\hat{\kappa}}}\right) q\sqrt{\hat{\kappa}} - \cosh\left(\frac{1}{\sqrt{\hat{\kappa}}}\right) q + 2\cosh\left(\frac{1}{\sqrt{\hat{\kappa}}}\right) - q - 2}{4\cosh\left(\frac{1}{\sqrt{\hat{\kappa}}}\right)\sqrt{\hat{\kappa}} - 2\sinh\left(\frac{1}{\sqrt{\hat{\kappa}}}\right) - 4\sqrt{\hat{\kappa}}},$$

$$c_2 = -2\frac{(1-q/2)\sinh\left(\frac{1}{\sqrt{\hat{\kappa}}}\right) + q\sqrt{\hat{\kappa}}\left(\cosh\left(\frac{1}{\sqrt{\hat{\kappa}}}\right) - 1\right)}{4\cosh\left(\frac{1}{\sqrt{\hat{\kappa}}}\right)\sqrt{\hat{\kappa}} - 2\sinh\left(\frac{1}{\sqrt{\hat{\kappa}}}\right) - 4\sqrt{\hat{\kappa}}},$$

$$c_3 = 2\frac{(1-q/2)\sinh\left(\frac{1}{\sqrt{\hat{\kappa}}}\right) + q\sqrt{\hat{\kappa}}\left(\cosh\left(\frac{1}{\sqrt{\hat{\kappa}}}\right) - 1\right)}{4\cosh\left(\frac{1}{\sqrt{\hat{\kappa}}}\right)\sqrt{\hat{\kappa}} - 2\sinh\left(\frac{1}{\sqrt{\hat{\kappa}}}\right) - 4\sqrt{\hat{\kappa}}},$$

$$c_4 = \frac{(d(q+2)\beta_t + 4T_U)\hat{\kappa}\cosh\left(\frac{1}{\sqrt{\hat{\kappa}}}\right) + \left(-2\hat{\kappa}^{3/2} dq\beta_t - 2\sqrt{\hat{\kappa}}(d\beta_t + T_U)\right)\sinh\left(\frac{1}{\sqrt{\hat{\kappa}}}\right)}{4\left(\hat{\kappa}\cosh\left(\frac{1}{\sqrt{\hat{\kappa}}}\right) - 1/2\sinh\left(\frac{1}{\sqrt{\hat{\kappa}}}\right)\sqrt{\hat{\kappa}} - \hat{\kappa}\right)\beta_t}$$
$$+ \frac{(d(q-2)\beta_t - 4T_U)\hat{\kappa}}{4\left(\hat{\kappa}\cosh\left(\frac{1}{\sqrt{\hat{\kappa}}}\right) - 1/2\sinh\left(\frac{1}{\sqrt{\hat{\kappa}}}\right)\sqrt{\hat{\kappa}} - \hat{\kappa}\right)\beta_t},$$

$$\hat{\kappa} = \frac{\kappa_{t2}}{d^2\kappa_{t1}}, \quad q = \frac{Q\,d}{\beta_t \kappa_{t1}}.$$

To advance the analysis, we recast the non-homogeneous equation (2.1) into a homogeneous form via a perturbation scheme. Accordingly, we perturb the base state $(\mathbf{u}, \bar{p}, \bar{T})$ by $(\mathbf{h}, \pi, \theta)$ and define the new variables as follows:

$$\mathbf{v} = \mathbf{u} + \mathbf{h}, \quad p = \bar{p} + \pi, \quad T = \bar{T} + \theta.$$

To make the perturbed system dimensionless and simplify the governing parameters, we propose the following typical scales:

$$L = d, \quad \bar{t} = \frac{d^2}{M\kappa_{t1}}, \quad \bar{h} = \frac{\kappa_{t1}}{d}, \quad \bar{\pi} = \frac{\mu\kappa_{t1}}{\kappa}, \quad \lambda = \frac{\tilde{\chi}\kappa}{d^2\mu}, \quad \bar{\theta} = \sqrt{\frac{\mu\kappa_{t1}\beta_t}{\rho_0 \mathrm{g} \varrho_T \kappa}}.$$

In this formulation, L denotes the characteristic length, $\bar{t}$ the characteristic time, $\bar{h}$ the reference velocity, $\bar{\pi}$ the reference pressure, and $\bar{\theta}$ the reference temperature. Moreover, λ is the Brinkman coefficient. The thermal Rayleigh number, R_t, is characterised by

$$R_t = \sqrt{\frac{\rho_0 g \varrho_T \kappa \, \beta_t \, d^2}{\mu \kappa_{t1}}}.$$

Non-dimensionalisation is essential for assessing the onset and development of convective instabilities. Using these non-dimensional scales, the linearised perturbation equations can be stated compactly as:

$$\begin{aligned} &-\mathbf{h} - \nabla\pi - \mathbf{k} R_t \theta + \lambda \Delta \mathbf{h} = 0, \\ &\frac{\partial \theta}{\partial t} + f(z) h_3 R_t + \mathbf{h} \cdot \nabla\theta = \Delta\theta - \hat{\kappa} \Delta^2 \theta, \end{aligned} \tag{2.4}$$

where the function $f(z)$ has the following formula:

$$f(z) = c_1 \sinh(\frac{z}{\sqrt{\hat{\kappa}}}) + c_2 \cosh(\frac{z}{\sqrt{\hat{\kappa}}}) + c_3 - zq. \tag{2.5}$$

In fact, (2.4) is defined within the space $\Psi_1 = \left\{(x, y, z, t) \in \mathbb{R}^2 \times (0, 1) \times R^+\right\}$. Moreover, the boundary conditions specified in equation (2.2) can be cast into the following nondimensional form:

$$h_i = 0, \quad \theta = 0, \quad \frac{\partial \theta}{\partial z} = 0, \qquad \text{at} \quad z = 0, 1. \tag{2.6}$$

3 Instability analysis

We first linearise (2.4) by removing its nonlinear terms, in order to study the instability thresholds:

$$\begin{aligned} &-\mathbf{h} - \nabla\pi - \mathbf{k} R_t \theta + \lambda \Delta \mathbf{h} = 0, \\ &\frac{\partial \theta}{\partial t} + f(z) h_3 R_t = \Delta\theta - \hat{\kappa} \Delta^2 \theta. \end{aligned} \tag{3.1}$$

Then, we adopt the normal–mode with exponential time dependence $e^{\sigma t}$, so that

$$\mathbf{h}(\mathbf{x}, t) = \mathbf{h}(\mathbf{x}) e^{\sigma t}, \;\; \pi(\mathbf{x}, t) = \pi(\mathbf{x}) e^{\sigma t}, \;\; \theta(\mathbf{x}, t) = \theta(\mathbf{x}) e^{\sigma t},$$

with σ a complex constant that denotes the growth rate. Hence, (3.1) simplifies to:

$$\begin{aligned} &-\mathbf{h} - \nabla\pi - \mathbf{k} R_t \theta + \lambda \Delta \mathbf{h} = 0, \\ &\sigma\theta + f(z) h_3 R_t = \Delta\theta - \hat{\kappa} \Delta^2 \theta. \end{aligned} \tag{3.2}$$

Our principal aim is to analyse the system's dependence on the parameter σ. Accordingly, we apply the double-curl operator to $(3.2)_1$ and retain its third component, which

yields the following linear system:

$$\begin{aligned} &\Delta h_3 + R_t \Delta^* \theta - \lambda \Delta^2 h_3 = 0, \\ &\sigma\theta + f(z) h_3 R_t = \Delta\theta - \hat{\kappa}\Delta^2\theta, \end{aligned} \tag{3.3}$$

where Δ^* represents the horizontal Laplacian, defined as $\Delta^* = \frac{\partial^2}{\partial x^2} + \frac{\partial^2}{\partial y^2}$. We subsequently express the system (3.3) in normal modes by establishing

$$h_3 = \Im(x,\ y) H_3(z), \theta = \Im(x,\ y)\Theta(z), \tag{3.4}$$

where $\Im(x,\ y)$ denotes a planar tiling form, defined such that

$$\Delta^* \Im(x,\ y) = -a^2\, \Im(x,\ y), \tag{3.5}$$

where a is a wavenumber, thus, it can be observed that

$$\begin{aligned} &(D^2 - a^2) H_3 - a^2 R_t \Theta - \lambda (D^2 - a^2)^2 H_3 = 0, \\ &\sigma\Theta + f(z) H_3 R_t = (D^2 - a^2)\Theta - \hat{\kappa}(D^2 - a^2)^2 \Theta. \end{aligned} \tag{3.6}$$

Where the boundary conditions for free-free surfaces become

$$H_3 = D^2 H_3 = 0, \quad \Theta = 0, \quad \frac{\partial \Theta}{\partial z} = 0, \qquad at\ \ z = 0, 1. \tag{3.7}$$

while for rigid-rigid surfaces, these take the form

$$H_3 = D H_3 = 0, \quad \Theta = 0, \quad \frac{\partial \Theta}{\partial z} = 0, \qquad at\ \ z = 0, 1. \tag{3.8}$$

If we adopt illustrative boundary conditions as in [45] then we may arrange (3.3) as

$$\begin{aligned} &L_1 h_3 \equiv \Delta h_3 - \lambda \Delta^2 h_3 = a^2 R_t \theta, \\ &L_2 \theta \equiv \sigma\theta - \Delta\theta + \hat{\kappa}\Delta^2\theta = -f(z) h_3 R_t. \end{aligned} \tag{3.9}$$

Then acting with the operator L_2 on the left of the first relation in (3.9) removes θ, giving the full equation for h_3:

$$\sigma h_3^* \Delta h_3 - (\sigma\lambda + 1) h_3^* \Delta^2 h_3 + (\lambda + \hat{\kappa}) h_3^* \Delta^3 h_3 - \hat{\kappa}\lambda h_3^* \Delta^4 h_3 = -a^2 R_t^2 f(z) h_3^* h_3. \tag{3.10}$$

Now multiply this equation by h_3^*, the complex conjugate of h_3, and integrate over a period cell V.

$$\begin{aligned}\sigma \int_V h_3^* \Delta h_3 dV - (\sigma\lambda + 1) \int_V h_3^* \Delta^2 h_3 dV + (\lambda + \hat{\kappa}) \int_V h_3^* \Delta^3 h_3 dV \\ - \hat{\kappa}\lambda \int_V h_3^* \Delta^4 h_3 dV = -a^2 R_c^2 \int_V f(z) h_3^* h_3 dV.\end{aligned} \tag{3.11}$$

This leads to the equation

$$\begin{aligned}\sigma(-\|\nabla h_3\|^2 - \lambda\|\Delta h_3\|^2) = \|\Delta h_3\|^2 + (\lambda + \hat{\kappa})\|\nabla \Delta h_3\|^2 + \hat{\kappa}\lambda \left\| \Delta^2 h_3 \right\|^2 \\ - a^2 R_c^2 \int_V f(z) h_3^* h_3 dV.\end{aligned} \tag{3.12}$$

Typically, the integrals on the right-hand side of (3.12) is complex-valued, which in turn forces the parameter σ to be complex.

4 Stability analysis

A nonlinear stability analysis is required to determine the exact conditions under which the system remains stable. To characterise the onset of convection, we employ the full nonlinear form of (2.4). Multiplying the first part of (2.4) by $\mathbf{h}$ and the second part by θ, and integrating each over the volume V, yields the following governing relations:

$$\begin{aligned}&-\|\mathbf{h}\|^2 - R_t(h_3, \theta) - \lambda\|\nabla \mathbf{h}\|^2 = 0, \\ &\frac{1}{2}\frac{d}{dt}\|\theta\|^2 + (\theta, f(z)h_3)R_t = -\|\nabla\theta\|^2 - \hat{\kappa}\|\Delta\theta\|^2.\end{aligned} \tag{4.1}$$

To investigate the system's nonlinear stability, we introduce the Lyapunov functional

$$E(t) = \frac{\bar{\lambda}}{2}\|\theta\|^2,$$

where $\bar{\lambda}$ is a fixed constant. Multiplying $(4.1)_1$ by unity and $(4.1)_2$ by $\bar{\lambda}$, and then summing, one obtains

$$\frac{dE}{dt} = I - D, \tag{4.2}$$

where

$$\begin{aligned}I &= -R_t(\theta, (1 + \bar{\lambda} f(z))h_3), \\ D &= \|\mathbf{h}\|^2 + \lambda\|\nabla \mathbf{h}\|^2 + \bar{\lambda}\|\nabla\theta\|^2 + \bar{\lambda}\hat{\kappa}\|\Delta\theta\|^2.\end{aligned} \tag{4.3}$$

Now define

$$\frac{1}{R_E} = \max_H \frac{I}{D}, \tag{4.4}$$

where H denotes the admissible solution set. Invoking (4.2) and (4.4), we obtain the following inequality:

$$\frac{dE}{dt} \leq -D(1 - \frac{1}{R_E}). \tag{4.5}$$

Under the assumption $\varsigma = 1 - \frac{1}{R_E}$ (with $R_E > 1$), Poincaré's inequality applied to (4.5) gives:

$$\frac{dE}{dt} \leq -2\varsigma bE, \tag{4.6}$$

where

$$b = \hat{\kappa}\pi^2 + \pi^4.$$

Upon time integration of the above inequality, we obtain $E(t) \leq E(0)\, e^{-2\varsigma bt}$. In particular $E(t) \to 0$ as $t \to \infty$; consequently $\|\theta(t)\| \to 0$.

To address the maximisation problem (4.4) under the constraint $R_E > 1$, we first consider the boundary case $R_E = 1$ and, by applying variational maximisation principles, deduce the following Euler-Lagrange equations:

$$\begin{aligned} -(1 + \bar{\lambda} f(z)) k_i R_t \theta - 2\mathbf{h} + 2\lambda \Delta \mathbf{h} &= \vartheta_{,i}\,, \\ -(1 + \bar{\lambda} f(z)) R_t h_3 + 2\bar{\lambda}\Delta\theta - 2\bar{\lambda}\hat{\kappa}\Delta^2\theta &= 0. \end{aligned} \tag{4.7}$$

The variable ϑ denotes the Lagrange multiplier. We will eliminate the Lagrange multipliers by choosing the third component of the double curl in $(4.7)_1$ and executing the normal mode

$$\mathbf{h} = \Im(x, y)\, H_3(z), \qquad \theta = \Im(x, y)\Theta(z),$$

to get

$$\begin{aligned} -(1 + \bar{\lambda} f(z)) a^2 R_t \Theta + 2(D^2 - a^2) H_3 - 2\lambda (D^2 - a^2)^2 H_3 &= 0, \\ -(1 + \bar{\lambda} f(z)) R_t H_3 + 2\bar{\lambda}(D^2 - a^2)\Theta - 2\bar{\lambda}\hat{\kappa}(D^2 - a^2)^2\Theta &= 0, \end{aligned} \tag{4.8}$$

together with the boundary conditions (3.7) and (3.8). This is an eigenvalue problem for the critical nonlinear Rayleigh number Ra_E, which is given by

$$Ra_E = \max_{\bar{\lambda}} \min_{a^2} R_t^2(a^2, \bar{\lambda}). \tag{4.9}$$

This study utilises numerical optimisation to calculate the nonlinear energy-stability threshold Ra_E by minimising the squared wavenumber a^2 while simultaneously maximising the parameter $\bar{\lambda}$.

5 Computational techniques

Numerical schemes that deliver high accuracy at modest computational cost are essential for the analysis of hydrodynamic instabilities. We adopt a Chebyshev-collocation framework in a shifted basis, which offers spectral accuracy, excellent boundary-layer resolution, and a compact algebraic structure. By expanding the unknown fields in tailored Chebyshev series and enforcing the governing equations at Gauss-Lobatto points, the method achieves high precision with comparatively few degrees of freedom. For background and related applications, see [30–33].

In this section we introduce and compare two Chebyshev–collocation formulations. Method I discretises the coupled momentum and heat equations, together with their boundary conditions, using the standard shifted–Chebyshev basis. Method II constructs boundary-fitted trial functions as linear combinations of three consecutive shifted–Chebyshev polynomials so that all boundary conditions are enforced identically. This removes the eight boundary rows and columns from the discrete system and substantially reduces its dimension. On these two discretisations we then build two complementary stability algorithms.

5.1 Method I: Standard shifted-Chebyshev collocation

Our starting point is to represent $H_3(z)$ and $\Theta(z)$ by truncated series in shifted Chebyshev bases, namely:

$$H_3(z) = \sum_{m=0}^{\mathrm{P}-1} c_m T_m(2z-1), \qquad \Theta(z) = \sum_{m=0}^{\mathrm{P}-1} c_{\mathrm{P}+m}\, T_m(2z-1), \tag{5.1}$$

where the Chebyshev polynomials (first kind) are given by $T_m(z) = \cos\big(m \arccos z\big)$. Substituting (5.1) into (3.6) yields:

$$\begin{aligned}
&\sum_{m=0}^{\mathrm{P}-1} \left(-16\lambda T_m^{(4)}(2z-1) + (4+8\lambda a^2) T_m''(2z-1) - (a^2+\lambda a^4) T_m(2z-1)\right) c_m \\
&- \sum_{m=0}^{\mathrm{P}-1} a^2 R_t\, T_m(2z-1)\, c_{\mathrm{P}+m} = 0, \\
&- \sum_{m=0}^{\mathrm{P}-1} \left(16\hat{\kappa} T_m^{(4)}(2z-1) - (8a^2\hat{\kappa}+4) T_m''(2z-1) + (a^4\hat{\kappa}+a^2) T_m(2z-1)\right) c_{\mathrm{P}+m} \\
&- \sum_{m=0}^{\mathrm{P}-1} f(z) R_t\, T_m(2z-1)\, c_m = \sigma \sum_{m=0}^{\mathrm{P}-1} c_{\mathrm{P}+m}\, T_m(2z-1).
\end{aligned} \tag{5.2}$$

We set $\mathrm{J_P} = \{1, 2, \ldots, \mathrm{P}\}$ and employ the Chebyshev–Gauss–Lobatto nodes

$$z_j = \cos\left(\frac{j-1}{\mathrm{P}-1}\pi\right), \qquad \forall j \in \mathrm{J_P}. \tag{5.3}$$

To set up the spectral problem, we collocate the first component of (5.2) at z_j for $j = 1, \ldots, \mathrm{P}-4$, while the fourth residual is obtained by enforcing the boundary conditions (3.7) (free-free) or (3.8) (rigid-rigid). Repeating the collocation for the second component of (5.2) with the same index set, and expressing the remaining equations via (3.7), furnishes an eigenvalue problem with spectral parameter σ and eigenvector $C = (c_0, c_1, \ldots, c_{2\mathrm{P}-1})^{\mathrm{T}}$.

$$\begin{pmatrix} \mathrm{M}_{(\mathrm{P}-4)\times\mathrm{P}} & \mathrm{X}_{(\mathrm{P}-4)\times\mathrm{P}} \\ \Upsilon_{4\times\mathrm{P}} & O_{4\times\mathrm{P}} \\ \mathrm{U}_{(\mathrm{P}-4)\times\mathrm{P}} & \Xi_{(\mathrm{P}-4)\times\mathrm{P}} \\ O_{4\times\mathrm{P}} & \mathrm{G}_{4\times\mathrm{P}} \end{pmatrix} \begin{pmatrix} c_0 \\ c_1 \\ \vdots \\ c_{2\mathrm{P}-1} \end{pmatrix} = \sigma \begin{pmatrix} O_{\mathrm{P}\times\mathrm{P}} & O_{\mathrm{P}\times\mathrm{P}} \\ O_{(\mathrm{P}-4)\times\mathrm{P}} & \mathrm{V}_{(\mathrm{P}-4)\times\mathrm{P}} \\ O_{4\times\mathrm{P}} & O_{4\times\mathrm{P}} \end{pmatrix} \begin{pmatrix} c_0 \\ c_1 \\ \vdots \\ c_{2\mathrm{P}-1} \end{pmatrix}, \tag{5.4}$$

where O denotes the zero matrix wherever it appears in (5.4), and

$$\begin{aligned}
\mathrm{M}_{n,m} =& -16\lambda T^{(4)}_{m-1}(2z_n-1) + (4+8\lambda a^2)T^{(2)}_{m-1}(2z_n-1) \\
& -(a^2+\lambda a^4)T_{m-1}(2z_n-1), && \forall m \in \mathrm{J_P},\ n \in \mathrm{J_{P-4}}, \\
\mathrm{X}_{n,m} =& -a^2 R_t T_{m-1}(2z_n-1), && \forall m \in \mathrm{J_P},\ n \in \mathrm{J_{P-4}}, \\
\Xi_{n,m} =& -16\hat{\kappa} T^{(4)}_{m-1}(2z_n-1) + (8a^2\hat{\kappa}+4)T^{(2)}_{m-1}(2z_n-1) \\
& -(a^4\hat{\kappa}+a^2)T_{m-1}(2z_n-1), && \forall m \in \mathrm{J_P},\ n \in \mathrm{J_{P-4}}, \\
\mathrm{U}_{n,m} =& -R_t f(z_n) T_{m-1}(2z_n-1), && \forall m \in \mathrm{J_P},\ n \in \mathrm{J_{P-4}}, \\
\mathrm{V}_{n,m} =& T_{m-1}(2z_n-1), && \forall m \in \mathrm{J_P},\ n \in \mathrm{J_{P-4}}, \\
\Upsilon_{1,m} =& 1, && \forall m \in \mathrm{J_P}, \\
\Upsilon_{2,m} =& (-1)^{m-1}, && \forall m \in \mathrm{J_P}, \\
\Upsilon_{3,m} =& \begin{cases} (m-1)^4 - (m-1)^2, & \text{free-free}, \\ (m-1)^2, & \text{rigid-rigid}, \end{cases} && \forall m \in \mathrm{J_P}, \\
\Upsilon_{4,m} =& \begin{cases} (-1)^{m-1}((m-1)^4 - (m-1)^2), & \text{free-free}, \\ (-1)^m (m-1)^2, & \text{rigid-rigid}, \end{cases} && \forall m \in \mathrm{J_P}, \\
\mathrm{G}_{1,\mathrm{m}} =& 1, && \forall m \in \mathrm{J_P}, \\
\mathrm{G}_{2,\mathrm{m}} =& (-1)^{m-1}, && \forall m \in \mathrm{J_P}, \\
\mathrm{G}_{3,\mathrm{m}} =& (m-1)^2, && \forall m \in \mathrm{J_P}, \\
\mathrm{G}_{4,\mathrm{m}} =& (-1)^m (m-1)^2, && \forall m \in \mathrm{J_P}.
\end{aligned}$$

On the other hand, we proceed to determine the critical Rayleigh number for the nonlinear system, Ra_E. Substituting (5.1) into (4.8) yields:

$$\begin{aligned}
&\sum_{m=0}^{\mathrm{P}-1} 2(-16\lambda T_m^{(4)}(2z-1) + (4+8\lambda a^2)T_m''(2z-1) - (a^2+\lambda a^4)T_m(2z-1))\, c_m \\
&-\sum_{m=0}^{\mathrm{P}-1} a^2 R_t(1+\bar{\chi} f(z))\, T_m(2z-1)\, c_{\mathrm{P}+m} = 0, \\
&-2\bar{\chi}\sum_{m=0}^{\mathrm{P}-1}(a^4\hat{\kappa}+a^2)T_m(2z-1)c_{\mathrm{P}+m} - \sum_{m=0}^{\mathrm{P}-1}(1+\bar{\chi} f(z))R_t\, T_m(2z-1)\, c_m \\
&-2\bar{\chi}\sum_{m=0}^{\mathrm{P}-1}(16\hat{\kappa}T_m^{(4)}(2z-1) - (8a^2\hat{\kappa}+4)T''_m(2z-1))\, c_{\mathrm{P}+m} = 0. \qquad (5.5)
\end{aligned}$$

To formulate the eigenvalue problem, we collocate (5.5) at the Gauss–Lobatto points z_j for $j = 0, \ldots, \mathrm{P}-4$; the remaining equations are supplied by the boundary conditions (3.7) (free–free) or (3.8) (rigid–rigid). Consequently, we obtain the following generalised eigenvalue problem, in which R_t is the eigenvalue and $C = (c_0, c_1, \ldots, c_{2\mathrm{P}-1})^{\mathrm{T}}$ denotes the corresponding eigenvector.

$$\begin{pmatrix} 2\mathrm{M}_{(\mathrm{P}-4)\times\mathrm{P}} & O_{(\mathrm{P}-4)\times\mathrm{P}} \\ \Upsilon_{4\times\mathrm{P}} & O_{4\times\mathrm{P}} \\ O_{(\mathrm{P}-4)\times\mathrm{P}} & \bar{\chi}\Xi_{(\mathrm{P}-4)\times\mathrm{P}} \\ O_{4\times\mathrm{P}} & \Theta_{4\times\mathrm{P}} \end{pmatrix} \begin{pmatrix} c_0 \\ c_1 \\ \vdots \\ c_{2\mathrm{P}-1} \end{pmatrix} = R_t \begin{pmatrix} O_{(\mathrm{P}-4)\times\mathrm{P}} & a^2 Q_{(\mathrm{P}-4)\times\mathrm{P}} \\ O_{4\times\mathrm{P}} & O_{4\times\mathrm{P}} \\ Q_{(\mathrm{P}-4)\times\mathrm{P}} & O_{(\mathrm{P}-4)\times\mathrm{P}} \\ O_{4\times\mathrm{P}} & O_{4\times\mathrm{P}} \end{pmatrix} \begin{pmatrix} c_0 \\ c_1 \\ \vdots \\ c_{2\mathrm{P}-1} \end{pmatrix}, \qquad (5.6)$$

where

$$\mathrm{Q}_{n,m} = (1+\bar{\chi} f(z_n))T_{m-1}(2z_n-1), \qquad \forall m \in \mathrm{J_P},\ n \in \mathrm{J_{P-4}}.$$

5.2 Method II: Boundary-fitted shifted-Chebyshev collocation

To reduce the matrix dimension relative to Method I, we construct trial spaces that satisfy all boundary conditions identically, thereby removing the eight rows and eight columns they contribute. Accordingly, we construct two Chebyshev-based families of trial functions, one for free-free and one for rigid-rigid boundary conditions, as follows:

$$\begin{aligned}
\psi_m^r(z) &= \sum_{i=0}^{2} \beta_{2i}\, T_{m+2i}(2z-1), \qquad m = 0, 1, 2, \ldots, \\
\psi_m^f(z) &= \sum_{i=0}^{2} \beta_{2i+1}\, T_{m+2i}(2z-1), \quad m = 0, 1, 2, \ldots,
\end{aligned} \qquad (5.7)$$

where

$$\beta_0 = 1, \quad \beta_2 = -2\frac{m+2}{m+3}, \qquad \beta_4 = \frac{m+1}{m+3},$$
$$\beta_1 = 1, \quad \beta_3 = -\frac{2(m+2)(2m^2+8m+15)}{(m+3)(2m^2+12m+19)}, \quad \beta_5 = \frac{(m+1)(2m^2+4m+3)}{(m+3)(2m^2+12m+19)}.$$

Indeed, each basis function $\psi_m^r(z)$, $\psi_m^f(z)$ is formed as a tailored linear combination of three successive shifted Chebyshev polynomials $\{T_m(2z-1), T_{m+2}(2z-1), T_{m+4}(2z-1)\}$. The coefficients are chosen so that the minematic (no-slip or stress-free) and thermal boundary operators vanish exactly at $z = 0, 1$, i.e. the constraints are embedded in the basis rather than enforced row-wise. So, the above basis functions satisfy the desired homogeneous boundary conditions for all $m \geq 0$:

$$\psi_m^f(0) = \psi_m^f(1) = 0, \qquad (D^2\psi_m^f)(0) = (D^2\psi_m^f)(1) = 0,$$
$$\psi_m^r(0) = \psi_m^r(1) = 0, \qquad (D\psi_m^r)(0) = (D\psi_m^r)(1) = 0.$$

Consequently, any finite expansion in $\{\psi_m^f\}_{m\geq 0}$ satisfies the free-free boundary conditions, and any finite expansion in $\{\psi_m^r\}_{m\geq 0}$ satisfies the rigid-rigid boundary conditions, thereby obviating additional boundary constraints in the algebraic system.

We then expand $H_3(z)$ and $\Theta(z)$ in the basis that matches the boundary condition under consideration. For rigid-rigid boundary conditions,

$$H_3(z) = \sum_{m=0}^{\mathrm{P}-1} c_m\, \psi_m^r(z), \qquad \Theta(z) = \sum_{m=0}^{\mathrm{P}-1} c_{\mathrm{P+m}}\, \psi_m^r(z). \tag{5.8}$$

For free-free boundary conditions,

$$H_3(z) = \sum_{m=0}^{\mathrm{P}-1} c_m\, \psi_m^f(z), \qquad \Theta(z) = \sum_{m=0}^{\mathrm{P}-1} c_{\mathrm{P+m}}\, \psi_m^r(z). \tag{5.9}$$

However, for the rigid–rigid case, substitute (5.8) into (3.6); for the free–free case, substitute (5.9) into (3.6) to obtain

$$\begin{aligned}
&\sum_{m=0}^{\mathrm{P}-1}\sum_{i=0}^{2}(-16\lambda T^{(4)}_{m+2i}(2z-1) + (4+8\lambda a^2)T''_{m+2i}(2z-1) - (a^2+\lambda a^4)T_{m+2i}(2z-1))\,\beta_{2i+J}\,c_m\\
&-\sum_{m=0}^{\mathrm{P}-1}\sum_{i=0}^{2} a^2 R_t\, T_{m+2i}(2z-1)\,\beta_{2i}\,c_{\mathrm{P+m}} = 0,\\
&-\sum_{m=0}^{\mathrm{P}-1}\sum_{i=0}^{2}(16\hat{\kappa}T^{(4)}_{m+2i}(2z-1) - (8a^2\hat{\kappa}+4)T''_{m+2i}(2z-1) + (a^4\hat{\kappa}+a^2)T_{m+2i}(2z-1))\,\beta_{2i}\,c_{\mathrm{P+m}}\\
&-\sum_{m=0}^{\mathrm{P}-1}\sum_{i=0}^{2} f(z)\,R_t\,T_{m+2i}(2z-1)\,\beta_{2i+J}\,c_m = \sigma\sum_{m=0}^{\mathrm{P}-1}\sum_{i=0}^{2}\beta_{2i}c_{\mathrm{P+m}}\,T_{m+2i}(2z-1),
\end{aligned} \tag{5.10}$$

where we set $\jmath = 0$ for the rigid–rigid case and $\jmath = 1$ for the free–free case. To formulate the eigenvalue problem, we insert the Gauss-Lobatto points, z_j, into (5.10) for $j \in \mathrm{P}-1$, Consequently, we formulated the subsequent generalised eigenvalue problem, wherein σ represents the eigenvalue and $C = (c_0, c_1, ..., c_{2\mathrm{P}-1})^{\mathrm{T}}$ denotes the eigenvector.

$$\begin{pmatrix} \mathrm{N}_{\mathrm{P}\times\mathrm{P}} & \mathrm{F}_{\mathrm{P}\times\mathrm{P}} \\ \mathrm{L}_{\mathrm{P}\times\mathrm{P}} & \mathrm{S}_{\mathrm{P}\times\mathrm{P}} \end{pmatrix} \begin{pmatrix} c_0 \\ c_1 \\ \vdots \\ c_{2\mathrm{P}-1} \end{pmatrix} = \sigma \begin{pmatrix} O_{\mathrm{P}\times\mathrm{P}} & O_{\mathrm{P}\times\mathrm{P}} \\ O_{\mathrm{P}\times\mathrm{P}} & \mathrm{Z}_{\mathrm{P}\times\mathrm{P}} \end{pmatrix} \begin{pmatrix} c_0 \\ c_1 \\ \vdots \\ c_{2\mathrm{P}-1} \end{pmatrix}, \tag{5.11}$$

where

$$\begin{aligned}
\mathrm{N}_{n,m} &= \sum_{i=0}^{2} (-16\lambda T^{(4)}_{m-1}(2z_n - 1) + (4 + 8\lambda a^2) T^{(2)}_{m-1}(2z_n - 1) \\
&\quad - (a^2 + \lambda a^4) T_{m-1}(2z_n - 1)) \, \beta_{2i+\jmath}, && \forall m, n \in \mathrm{J_P}, \\
\mathrm{F}_{n,m} &= -\sum_{i=0}^{2} a^2 R_t T_{m-1}(2z_n - 1) \, \beta_{2i}, && \forall m, n \in \mathrm{J_P}, \\
\mathrm{L}_{n,m} &= \sum_{i=0}^{2} f(z_n) R_t T_{m+2i}(2z_n - 1) \, \beta_{2i+\jmath}, && \forall m, n \in \mathrm{J_P}, \\
\mathrm{S}_{n,m} &= \sum_{i=0}^{2} (16\hat{\kappa} T^{(4)}_{m+2i}(2z_n - 1) - (8a^2\hat{\kappa} + 4) T''_{m+2i}(2z_n - 1) \\
&\quad + (a^4\hat{\kappa} + a^2) T_{m+2i}(2z_n - 1)) \, \beta_{2i}, && \forall m, n \in \mathrm{J_P}, \\
\mathrm{Z}_{n,m} &= \sum_{i=0}^{2} \beta_{2i} T_{m+2i}(2z_n - 1), && \forall m, n \in \mathrm{J_P}.
\end{aligned} \tag{5.12}$$

We now turn to the nonlinear problem and the associated critical Rayleigh number Ra_E. For the rigid–rigid case, we substitute (5.8) into (4.8); for the free–free case, we substitute (5.9) into (4.8). These substitutions yield:

$$\begin{aligned}
&\sum_{m=0}^{\mathrm{P}-1} \sum_{i=0}^{2} 2(-16\lambda T^{(4)}_{m+2i}(2z - 1) + (4 + 8\lambda a^2) T''_{m+2i}(2z - 1) - (a^2 + \lambda a^4) T_{m+2i}(2z - 1)) \, \beta_{2i+\jmath} \, c_m \\
&- \sum_{m=0}^{\mathrm{P}-1} a^2 R_t (1 + \bar{\chi} f(z)) T_{m+2i}(2z - 1) \, \beta_{2i} \, c_{\mathrm{P}+m} = 0, \\
&-2\chi \sum_{m=0}^{\mathrm{P}-1} \sum_{i=0}^{2} (a^4\hat{\kappa} + a^2) T_{m+2i}(2z - 1) \beta_{2i} c_{\mathrm{P}+m} - \sum_{m=0}^{\mathrm{P}-1} \sum_{i=0}^{2} (1 + \bar{\chi} f(z)) R_t T_{m+2i}(2z - 1) \; \beta_{2i+\jmath} c_m \\
&-2\chi \sum_{m=0}^{\mathrm{P}-1} \sum_{i=0}^{2} (16\hat{\kappa} T^{(4)}_{m+2i}(2z - 1) - (8a^2\hat{\kappa} + 4) T''_{m+2i}(2z - 1)) \, \beta_{2i} \, c_{\mathrm{P}+m} = 0.
\end{aligned} \tag{5.13}$$

We set $\jmath = 0$ for the rigid-rigid configuration and $\jmath = 1$ for the free-free configuration. Collocating (5.13) at the Gauss-Lobatto nodes z_j for $j = 0, \ldots, \mathrm{P}-1$ yields the following generalised eigenvalue problem, with R_t as the eigenvalue and $C = (c_0, c_1, \ldots, c_{2\mathrm{P}-1})^{\mathrm{T}}$ as the corresponding eigenvector.

$$\begin{pmatrix} 2\mathrm{N}_{\mathrm{P}\times\mathrm{P}} & O_{\mathrm{P}\times\mathrm{P}} \\ O_{\mathrm{P}\times\mathrm{P}} & 2\bar{\lambda}\mathrm{S}_{\mathrm{P}\times\mathrm{P}} \end{pmatrix} \begin{pmatrix} c_0 \\ c_1 \\ \vdots \\ c_{2\mathrm{P}-1} \end{pmatrix} = R_t \begin{pmatrix} O_{\mathrm{P}\times\mathrm{P}} & \Phi_{\mathrm{P}\times\mathrm{P}} \\ \Pi_{\mathrm{P}\times\mathrm{P}} & O_{\mathrm{P}\times\mathrm{P}} \end{pmatrix} \begin{pmatrix} c_0 \\ c_1 \\ \vdots \\ c_{2\mathrm{P}-1} \end{pmatrix}, \tag{5.14}$$

where

$$\Phi_{n,m} = \sum_{i=0}^{2} (1 + \bar{\lambda} f(z_{n-1})) T_{m+2i}(2z_{n-1} - 1)\, \beta_{2i}, \qquad \forall m \in \mathrm{J_P},\ n \in \mathrm{J_P},$$

$$\Pi_{\mathrm{P}\times\mathrm{P}} = \sum_{i=0}^{2} (1 + \bar{\lambda} f(z_{n-1})) T_{m+2i}(2z_{n-1} - 1)\, \beta_{2i+\jmath}, \quad \forall m \in \mathrm{J_P},\ n \in \mathrm{J_P}.$$

5.3 Two Algorithms for Ra_L and Ra_E

In light of the derived results of the two methods, and to facilitate and offer summaries of the numerical computations, we have introduced two algorithms for computing Ra_L and Ra_E. The computation of Ra_L using Methods I and II is carried out in accordance with Algorithm 1.

Algorithm 1 Algorithm for Linear Instability

Input: Chebyshev polynomials of order P, along with the physical parameters $\hat{\kappa}$, a, q, and λ.
Output: Critical Rayleigh number Ra_L.

1: Determine the Gauss-Lobatto nodes $\{z_j\}$ using (5.3).
2: For a prescribed wavenumber a, construct the block matrices in Method I (5.4) or Method II (5.11), and cast the resulting discretised system into the generalised eigenvalue form $\mathbf{A}\,\mathbf{c} = \sigma\,\mathbf{B}\,\mathbf{c}$.
3: Find the Moore-Penrose inverse $\mathbf{A}^{+}$ [38].
4: Calculate the eigenvalues of the matrix $\mathbf{A}^{+}\mathbf{B}$, denoted as $\{\ell_\kappa\}$, and define $\sigma_\kappa = 1/\ell_\kappa$ for $\ell_\kappa \neq 0$.
5: **Stationary branch:** Select real modes $\mathcal{S} = \{\sigma_\kappa : \mathrm{Im}(\sigma_\kappa) = 0\}$ and define $\sigma_{\mathrm{ST}}(R_t, a) = \min_{\sigma\in\mathcal{S}} \mathrm{Re}(\sigma)$.
6: For a fixed value of a, determine $R_t^{\mathrm{ST}}(a)$ such that $\sigma_{\mathrm{ST}}(R_t^{\mathrm{ST}}(a), a) = 0$ using the secant method.
7: Obtain $a^* = \min_a R_t^{\mathrm{ST}}(a)$ using the golden-section search method, and define $R_t^{\mathrm{ST}^*} = R_t^{\mathrm{ST}}(a^*)$.
8: **Oscillatory branch:** Select complex modes $\mathcal{O} = \{\sigma_\kappa : \mathrm{Im}(\sigma_\kappa) \neq 0\}$ and define $\sigma_{\mathrm{OS}}(R_t, a) = \min_{\sigma\in\mathcal{O}} \mathrm{Re}(\sigma)$.
9: For a fixed value of a, compute $R_t^{\mathrm{OS}}(a)$ such that $\sigma_{\mathrm{OS}}(R_t^{\mathrm{OS}}(a), a) = 0$ using the secant method.
10: Calculate $\tilde{a} = \min_a R_t^{\mathrm{OS}}(a)$ using the golden-section search method, and assign $R_t^{\mathrm{OS},*} = R_t^{\mathrm{OS}}(\tilde{a})$.
11: Calculate the global threshold

$$Ra_L = \min\{R_t^{\mathrm{ST}^*},\ R_t^{\mathrm{OS}^*}\}.$$

The computation of Ra_E via Methods I and II proceeds as outlined in Algorithm 2.

Algorithm 2 Stability algorithm

Input: P the truncation order of the Chebyshev expansion, physical parameters $\hat{\kappa}$, a, q, and λ.
Output: Critical Rayleigh number Ra_E.
1: Determine Gauss-Lobatto nodes $\{z_j\}$ via (5.3).
2: Assemble the block matrices in Method I (5.6) or Method II (5.14), for a specified wavenumber a and assume it by $\mathbf{A}\,\mathbf{c} = R_t\,\mathbf{B}\,\mathbf{c}$.
3: Compute the Moore-Penrose inverse $\mathbf{A}^+$ [38].
4: Calculate the eigenvalues of the matrix $\mathbf{A}^+\,\mathbf{B}$, say $\{\ell_\kappa\}$.
5: Choose the minimum value of $\left\{\mathrm{Re}\{\frac{1}{\ell_\kappa}\} \,\middle|\, \mathrm{Im}\{\frac{1}{\ell_\kappa}\} = 0 \;\&\; \ell_\kappa \neq 0\right\}$, denoted as $R_t^*(a^2,\bar{\lambda})$.
6: Determine $Ra_E = \max_{\bar{\lambda}}\left[\min_{a^2} R_t^*(a^2,\bar{\lambda})\right]$ by nested golden-section searches over a^2 (inner) and $\bar{\lambda}$ (outer).

5.4 Residual evaluation

Because no closed-form solution is available, we assess both Chebyshev-collocation formulations, Method I (standard basis) and Method II (boundary-satisfying trial functions), using a unified residual audit. Algorithm 3 evaluates interior and boundary defects and reports the mean residual over [0, 1]. For each P, we assemble and solve both discrete problems under identical settings and record the mean residual together with the matrix size, enabling a like-for-like comparison of accuracy versus complexity.

Algorithm 3 Residual-Based Evaluation of the Chebyshev Collocation Method for the Critical Rayleigh Number

Input: P, the truncation order of the Chebyshev expansion; the physical parameters of the eigenvalue problem; the critical Rayleigh number Ra_L; and the corresponding wavenumber a.
Output: The global L^2-norm of the residual, $\|\mathrm{Res}\|_2$.
1: Invoke Algorithm 1 to compute the critical Rayleigh number Ra_L, the associated wavenumber a, and the eigenvalue σ.
2: Assemble the Chebyshev collocation matrices $\mathbf{A}(Ra_L, a)$ and $\mathbf{B}$ such that

$$\mathbf{A}(Ra_L, a)\,C \;=\; \sigma\,\mathbf{B}\,C.$$

3: Impose $c_0 = 1$, and solve the above resulting linear system for the coefficients $c_1, c_2, \ldots, c_{2\mathrm{P}-1}$.
4: Substitute the computed expansions $H_3(z)$ and $\Theta(z)$, obtained using Method I or Method II, into (3.6), and subsequently evaluate the residual $\mathrm{Res}(z_j)$ at each collocation point z_j.
5: Compute the global L^2-norm of the residual:

$$\|\mathrm{Res}\|_2 \;=\; \left(\int_0^1 \left|\mathrm{Res}(z)\right|^2 dz\right)^{1/2}.$$

Table 2 Average residual value for method I with $\hat{\kappa} = 0.1$ and $q = 5$ in case free-free

λ	P = 70	P = 80	P = 90	P = 100
0.001	1.7076E-08	4.22231E-10	2.0745E-13	1.55951E-14
0.002	6.16573E-09	1.29709E-10	7.90323E-13	1.11375E-15
0.003	3.94494E-09	2.54213E-11	5.5514E-13	4.29575E-16
0.004	3.07088E-09	2.9475E-11	2.51588E-13	2.53789E-16
0.005	2.62803E-09	1.75445E-10	1.3823E-13	1.80496E-16
0.006	2.37362E-09	1.09148E-09	8.55274E-14	1.4269E-16
0.007	2.21451E-09	2.61655E-10	5.63374E-14	1.20532E-16
0.008	2.10941E-09	1.85429E-10	3.81464E-14	1.06526E-16
0.009	2.03551E-09	1.57956E-10	2.56955E-14	9.71602E-17
0.01	1.98108E-09	1.4471E-10	1.65946E-14	9.07133E-17

Table 3 Average residual value for method I with $\hat{\kappa} = 0.1$ and $q = 5$ in case rigid-rigid

λ	P = 70	P = 80	P = 90	P = 100
0.001	1.98851E-08	3.29499E-10	3.57857E-13	4.94413E-15
0.002	1.02711E-08	2.33301E-09	1.21594E-13	5.80569E-15
0.003	8.06012E-09	2.52427E-10	1.67335E-13	3.31728E-15
0.004	7.21883E-09	1.22178E-10	3.5246E-13	2.53383E-15
0.005	6.86629E-09	8.48335E-11	6.15457E-13	2.22324E-15
0.006	6.73571E-09	6.78069E-11	9.0487E-13	2.10999E-15
0.007	6.72202E-09	5.83636E-11	1.20328E-12	2.10379E-15
0.008	6.77968E-09	5.24567E-11	1.51624E-12	2.16932E-15
0.009	6.88588E-09	4.85836E-11	1.85065E-12	2.293E-15
0.01	7.0238E-09	4.5933E-11	2.21867E-12	2.47166E-15

Tables 2,3,4,5 show monotone decay of the average residual with P under both boundary types. For the same target residual, Method II typically requires about half the P used by Method I, reducing matrix size and cost while preserving the eigenpairs within numerical tolerance.

6 Parametric study of stability analysis

In this section we examine how the dimensionless parameters $\hat{\kappa}$, λ, and q shape the stability boundaries of a horizontally extended fluid layer. The linear onset of convection is determined by an eigenvalue (normal-mode) analysis; we will ascertain critical thresholds Ra. Nonlinear (finite-amplitude) thresholds are established using the energy method. We consider two velocity boundary conditions, stress-free and no-slip, and quantify their influence on Ra, on the energy-stability limit, and on the associated modal structure.

Table 4 Average residual value for method II with $\hat{\kappa} = 0.1$ and $q = 5$ in case free-free

λ	P = 35	P = 40	P = 45	P = 50
0.1	5.92703E-12	6.83428E-15	7.18377E-18	4.13552E-21
0.2	1.04392E-11	9.25487E-15	1.05027E-17	5.61492E-21
0.3	1.49805E-11	1.15109E-14	1.38369E-17	9.43702E-21
0.4	1.95288E-11	1.36619E-14	1.71643E-17	9.13213E-21
0.5	2.408E-11	1.57472E-14	2.04784E-17	1.12445E-20
0.6	2.86326E-11	1.77886E-14	2.37911E-17	1.55812E-20
0.7	3.3186E-11	1.97992E-14	2.70976E-17	2.13809E-20
0.8	3.77399E-11	2.17873E-14	3.04018E-17	2.55479E-20
0.9	4.22941E-11	2.37583E-14	3.3698E-17	2.40255E-20
1	4.68486E-11	2.5716E-14	3.70088E-17	3.14168E-20

Table 5 Average residual value for method II with $\hat{\kappa} = 0.1$ and $q = 5$ in case rigid-rigid

λ	P = 35	P = 40	P = 45	P = 50
0.1	1.16035E-10	1.82989E-13	1.50335E-16	1.84372E-18
0.2	1.99263E-10	3.15631E-13	2.71548E-16	2.97151E-18
0.3	2.82627E-10	4.48727E-13	3.92247E-16	7.8685E-18
0.4	3.65999E-10	5.81909E-13	5.1855E-16	1.45835E-18
0.5	4.49369E-10	7.15123E-13	6.38735E-16	1.6789E-18
0.6	5.32735E-10	8.48348E-13	7.68907E-16	8.38833E-18
0.7	6.16099E-10	9.81579E-13	8.87393E-16	1.81938E-17
0.8	6.99461E-10	1.11481E-12	1.00317E-15	1.23257E-17
0.9	7.82822E-10	1.24805E-12	1.12453E-15	1.12195E-17
1	8.66182E-10	1.38129E-12	1.25482E-15	3.87874E-18

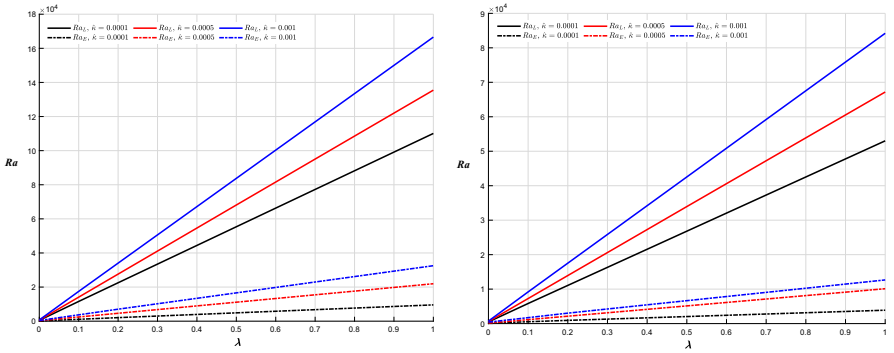

(a) Rigid-rigid case. (b) Free–free case.

Fig. 2 Plot of Ra against λ with $q = 5$ for various values of $\hat{\kappa}$

In Fig. 2, we examine the onset structure in terms of the Brinkman coefficient λ, the hyper–diffusion parameter $\hat{\kappa}$, and the prescribed internal heat source q. Here we use different colours to denote different hyper–diffusionlevels $\hat{\kappa}$, while line styles distinguish the two boundaries: dashed curves represent the stability boundary $Ra_E(\lambda; \hat{\kappa})$, and solid curves represent the instability boundary $Ra_L(\lambda; \hat{\kappa})$. For any fixed $\hat{\kappa}$, the dashed curve $Ra_E(\lambda; \hat{\kappa})$ lies below the solid curve $Ra_L(\lambda; \hat{\kappa})$ across the entire plotted λ range, thereby partitioning the (λ, Ra) parameter plane into three dynamically distinct regimes: stable ($Ra < Ra_E$), critical ($Ra_E \leq Ra \leq Ra_L$), and unstable ($Ra > Ra_L$). Across the ranges shown, both boundaries rise almost linearly with λ and shift upward as $\hat{\kappa}$ increases, demonstrating that Brinkman drag and hyper–diffusion act cooperatively to delay the onset of convection. A slope based reading of the curves indicates that the sensitivity with respect to λ is larger for the instability boundary than for the stability boundary. So that the width of the critical band, the vertical separation between the solid and dashed curves of the same colour, widens with λ. Physically, increasing λ enhances Brinkman drag, raising both thresholds and impeding buoyant motion, while increasing $\hat{\kappa}$ strengthens small scale diffusion, further suppressing nascent convective cells and shifting both boundaries upward.

However, at fixed $(\lambda, \hat{\kappa})$, every pair $\{Ra_E, Ra_L\}$ shifts upward when the boundary condition changes from free–free to rigid–rigid. Rigid walls generate additional shear and wall friction, which increase viscous dissipation and delay the onset of convection. As a result, the free–free panel shows lower dashed and solid levels (earlier onset), whereas the rigid–rigid panel places both the dashed stability boundary and the solid instability boundary at higher Ra. Taken together, Brinkman drag λ and hyperdiffusion $\hat{\kappa}$ raise both boundaries; the instability boundary is more responsive to λ; and rigid walls are uniformly more stabilising than stress–free ones.

In Fig. 3, we examine the onset structure in terms of the Brinkman coefficient λ at a fixed hyper–diffusion level $\hat{\kappa} = 10^{-4}$ and several prescribed internal heat sources q. Colours distinguish the different q values, while line styles distinguish the two boundaries: dashed curves represent the stability boundary $Ra_E(\lambda; q)$ and solid curves represent the instability boundary $Ra_L(\lambda; q)$. For any fixed q, the dashed curve $Ra_E(\lambda; q)$ lies below the solid curve $Ra_L(\lambda; q)$ across the entire plotted λ range, thereby partitioning the (λ, Ra) plane into three dynamically distinct regimes: stable ($Ra < Ra_E$), critical ($Ra_E \leq Ra \leq Ra_L$), and unstable ($Ra > Ra_L$). Across the ranges shown, both boundaries grow almost linearly with λ. Their placement depends monotonically on the heat source: increasing q shifts both boundaries downward, indicating that stronger internal heating destabilises the layer and triggers convection at lower Ra. The slope of the solid lines exceeds that of the dashed lines, indicating that the instability threshold Ra_L is more λ-sensitive than the stability threshold Ra_E; consequently, the critical band, the vertical separation between same-colour solid and dashed lines, widens as λ increases. Physically, increasing λ enhances Brinkman drag and delays the onset by raising both thresholds, whereas increasing q augments buoyancy production and lowers both thresholds.

In addition, at fixed $(\lambda, \hat{\kappa}, q)$, every pair $\{Ra_E, Ra_L\}$ shifts upward when the boundary condition changes from free–free to rigid–rigid. Rigid walls generate additional shear and wall friction, which increase viscous dissipation and delay the onset of convection. Consequently, the free–free panel shows lower dashed and solid levels (earlier

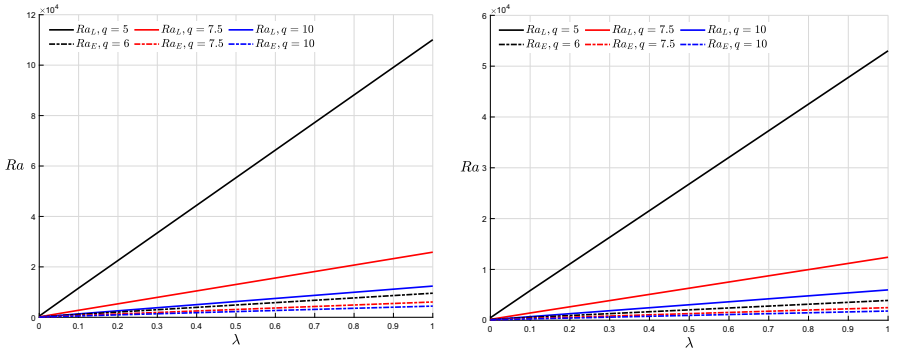

(a) Rigid-rigid case. (b) Free-free case.

Fig. 3 Plot of Ra against λ with $\hat{\kappa} = 0.0001$ for various values of q

onset), whereas the rigid–rigid panel places both the dashed stability boundary and the solid instability boundary at higher Ra. Taken together, Brinkman drag λ and internal heating q act in opposite directions, λ stabilises while q destabilises, while rigid walls are uniformly more stabilising than stress–free ones.

In Fig. 4 we plot the onset thresholds versus the internal heat source q at fixed hyper–diffusion $\hat{\kappa} = 10^{-4}$ for several Brinkman drags λ. Colours encode λ; dashed curves show the energy stability threshold $Ra_E(q;\lambda)$ and solid curves the linear instability threshold $Ra_L(q;\lambda)$. For each λ, Ra_L falls sharply as q increases. The decay is convex, steep at moderate q and flattening at larger q, because added heating strengthens buoyancy production until diffusion and Brinkman drag limit further gain. In contrast, Ra_E depends only weakly on q and drifts slightly upward; the near-linear appearance is a plotting artefact caused by the large vertical scale. From the energy perspective, increasing q enhances base state gradients and the production term in the energy inequality, so ensuring monotone decay for all admissible disturbances requires a modest increase in Ra_E.

Increasing λ shifts both thresholds upward across all q, with a much stronger impact on Ra_L. Brinkman drag acts as a momentum sink: it suppresses shear and reduces the conversion of potential to kinetic energy, delaying the most unstable eigenmode and raising Ra_L; the same mechanism lifts Ra_E, though by a smaller amount because dissipation is already built into the energy method. At fixed (q, λ), the rigid-rigid panel lies above the free-free panel for both thresholds. No-slip walls generate near-wall shear and extra viscous dissipation, reduce wall normal slip that would feed rolls, and therefore demand a larger Ra to initiate motion. In summary, internal heating q destabilises, Brinkman drag λ stabilises, and rigid boundaries further stabilise the layer; among the two thresholds, Ra_L is consistently more sensitive to λ.

To assess how thermal diffusion and internal heating affect the onset of convection, Fig. 5 fixes the Brinkman parameter at $\lambda = 0.5$ and plots the linear-instability boundary $Ra_L(\hat{\kappa}, q)$ and the energy-stability boundary $Ra_E(\hat{\kappa}, q)$ as the scaled hyper-diffusivity varies over $\hat{\kappa} \in (0,\ 2.5 \times 10^{-3}]$ and the nondimensional heat-generation rate takes values $q \in \{4,\ 4.5,\ 5\}$.

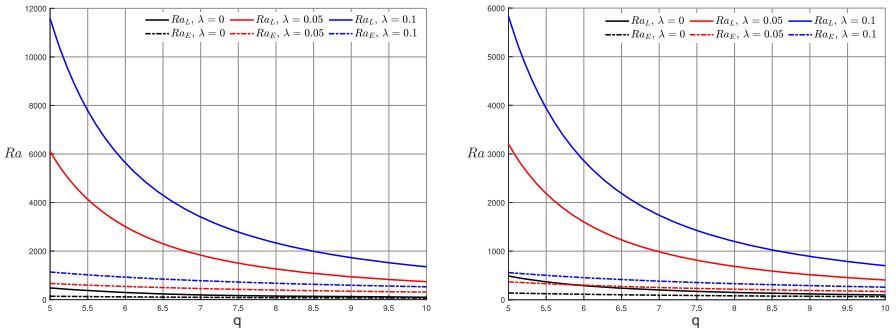

(a) Rigid-rigid case.

(b) Free-free case.

Fig. 4 Plot of Ra_L against q with $\hat{\kappa} = 0.0001$ for various values of λ

For every heating level q, Ra_L increases monotonically with $\hat{\kappa}$ for both boundary types. This rise reflects the increasing effectiveness of short-wavelength damping penalised by $\hat{\kappa}$, so a larger thermal Rayleigh number is required to trigger instability. The ordering with respect to heating is consistent: $q = 4$ yields the largest Ra_L, $q = 4.5$ is intermediate, and $q = 5$ is the smallest; hence stronger internal heating lowers the instability threshold, $\partial Ra_L/\partial q < 0$, by enhancing background buoyancy.

By contrast, Ra_E depends only weakly on $\hat{\kappa}$ and shifts mildly and almost in parallel with q; across the plotted range, Ra_E is one to two orders of magnitude below Ra_L. Consequently, the critical band $Ra_E \leq Ra \leq Ra_L$ widens with $\hat{\kappa}$, indicating greater separation between energy stability and linear instability at higher hyper-diffusion. Boundary conditions have a clear effect: rigid-rigid walls place both thresholds substantially higher than free-free walls, with about a twofold increase in Ra_L at representative $\hat{\kappa}$, because added wall friction and shear production delay both the initial (energy) and long-wave (linear) loss of stability.

In summary, increasing $\hat{\kappa}$ strongly stabilises the system through a convex increase of Ra_L (and only weakly of Ra_E); increasing q mainly destabilises by lowering Ra_L; and rigid-rigid boundaries are uniformly more stabilising than free-free boundaries for all $(\hat{\kappa}, q)$.

In Fig. 6 we examine the linear instability and energy stability thresholds under rigid-rigid and free-free velocity boundaries by plotting Ra against the internal heating rate q at fixed Brinkman drag $\lambda = 0.5$ for $\hat{\kappa} \in \{10^{-4},\ 5\times 10^{-4},\ 10^{-3}\}$. Increasing q lowers the critical thermal forcing: the buoyancy source in the heat equation scales with q, so perturbations extract energy more readily and Ra_L decreases monotonically, whereas the energy bound Ra_E is much less responsive because it derives from a global dissipation-production inequality rather than the first unstable eigenmode. By contrast, enlarging the hyper-diffusion $\hat{\kappa}$ raises both Ra_L and Ra_E; the bi-Laplacian strengthens short-wavelength damping in the temperature field, suppressing modal growth and tightening the nonlinear stability estimate. Rigid walls are more stabilising than stress-free boundaries, since the Darcy-Brinkman momentum balance incurs greater viscous dissipation at no-slip interfaces; hence all thresholds rise when moving from free-free to rigid-rigid conditions. Throughout the parameter range $Ra_E < Ra_L$, as expected

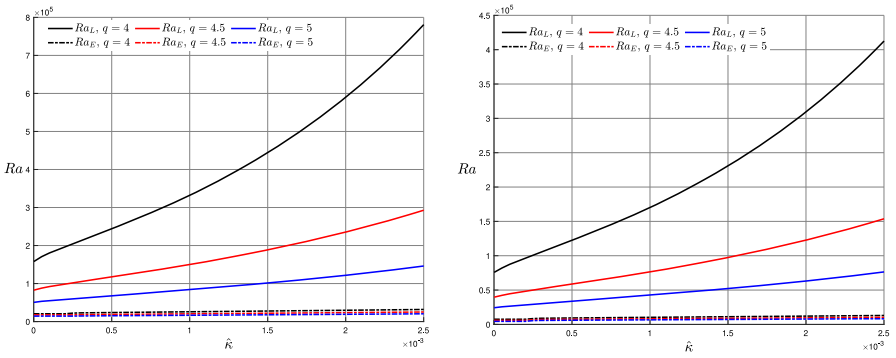

(a) Rigid-rigid case. (b) Free-free case.

Fig. 5 Plot of Ra against $\hat{\kappa}$ with $\lambda = 0.5$ for various values of q

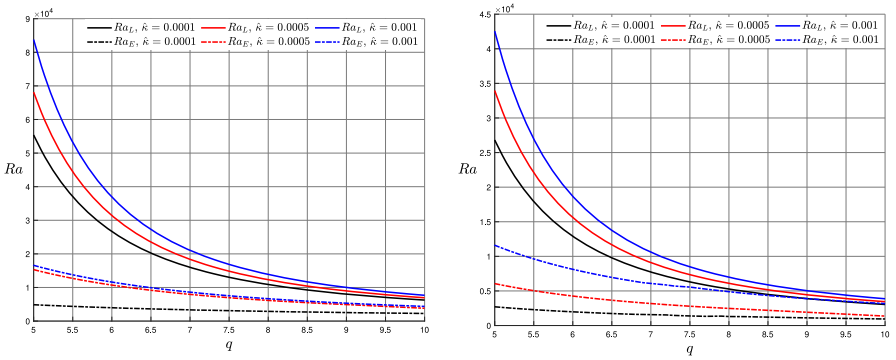

(a) Rigid-rigid case. (b) Free-free case.

Fig. 6 Plot of Ra against q with $\lambda = 0.5$ for various values of $\hat{\kappa}$

for a sufficient stability criterion. The critical region between these thresholds widens with $\hat{\kappa}$-eigenmodes are penalised more strongly than the global energy inequality-and narrows as q increases, because internal heating preferentially promotes modal amplification relative to the conservative energy bound. Overall, q promotes convection by boosting buoyancy production, whereas $\hat{\kappa}$ and wall friction (via Brinkman parameter) inhibit it by increasing dissipation.

7 Conclusions

Thermal convection in a horizontal porous layer governed by the Darcy-Brinkman equations with internal volumetric heating and higher-order temperature gradients presents a challenging stability problem with direct relevance to geothermal reservoirs, catalytic reactors and subsurface transport. Accurately predicting the onset of convection under such complex constitutive effects is crucial for designing efficient thermal management strategies and understanding natural convective phenomena.

To this end, we have developed and compared two Chebyshev-collocation formulations. The first employs shifted Chebyshev polynomials to discretise the coupled momentum and heat equations, while the second constructs trial functions from a linear combination of three different orders of shifted Chebyshev polynomials that identically satisfy all boundary conditions, thereby removing eight boundary rows and columns and substantially reducing the discrete problem dimension. Based on these two methods, we have implemented two complementary stability algorithms. The linear instability solver uses a spectral eigenvalue formulation to locate the critical Rayleigh number Ra_L, whereas the nonlinear energy-stability solver applies the Moore-Penrose pseudoinverse together with a golden-section search and eigenvalue-tracking procedure to determine the energy threshold Ra_E. A residual method is used to determine which method is more effective. In fact, it depends on computing the average spectral residual over both interior and boundary conditions as the number of trial functions varies, providing a systematic measure of accuracy versus computational cost for each formulation.

The parametric trends observed in Section 6 can be understood by examining how each non-dimensional parameter modifies the balance between buoyant driving and dissipative losses in the porous layer. The Brinkman coefficient λ represents the strength of viscous resistance imposed by the porous structure on fluid motion. As λ increases, the Darcy-Brinkman momentum equation acquires a larger momentum-sink term, so that any incipient convective roll must overcome greater frictional losses. Consequently, both the linear threshold Ra_L and the energy-stability threshold Ra_E increase almost linearly with λ, and the slope of $Ra_L(\lambda)$ exceeds that of $Ra_E(\lambda)$ because the eigenvalue calculation isolates the most unstable perturbation mode, which is especially sensitive to additional drag.

The hyper-diffusion parameter $\hat{\kappa}$ enters the heat equation via fourth-order derivatives, and physically it acts to smooth out small-scale temperature variations more strongly than the standard Laplacian term. When $\hat{\kappa}$ is larger, any fine-scale thermal perturbation is rapidly attenuated before it can organise into a buoyant plume. This increased thermal smoothing raises both Ra_E and Ra_L by suppressing the growth of high-wavenumber modes, and it shifts the entire stability envelope upward without altering its linear dependence on λ.

In contrast, the internal heat-source parameter q quantifies the volumetric generation of thermal energy within the layer. A larger q injects buoyancy directly into the base state, reducing the amount of externally imposed temperature difference required to trigger convection. As a result, increasing q causes both thresholds to decrease, with the linear threshold Ra_L exhibiting a steeper drop than Ra_E for moderate q; this is because the energy criterion averages perturbation fields globally, making it less sensitive to localised heating than the eigenvalue formulation.

The study consists of two scenarios of velocity boundary conditions that further modulate these effects by altering near-wall shear and thermal boundary-layer structure. Stress-free walls allow slip and minimise viscous dissipation at the boundaries, so the thresholds under free–free conditions lie below those for no–slip (rigid–rigid) walls. In the rigid–rigid case, the no–slip constraint enforces zero velocity at both boundaries, generating strong shear layers that dissipate perturbation energy and delay the onset of both linear and nonlinear instabilities. Together, these physical mecha-

nisms explain the widening of the critical band ($Ra_E \leq Ra \leq Ra_L$) at high λ, the downward shift of both thresholds with increasing q, and the uniformly stabilising role of $\hat{\kappa}$ and rigid boundaries. This insight underscores the interplay between momentum dissipation, thermal diffusion and buoyancy generation in controlling the complex onset of convection in porous media with internal heating and higher–order gradients.

Funding No funding has been received for this article.

Declarations

Conflicts of Interest We have no competing interests.

References

1. Abdul-Wahhab, R.D., Eisa, M.M., Khalaf, S.L.: The study of stability analysis of the ebola virus via fractional model. Partial Differential Equations in Applied Mathematics **11**, 100792 (2024). https://doi.org/10.1016/j.padiff.2024.100792
2. Arnone, G., Capone, F., De Luca, R., Gianfrani, J.A., Iovanna, F.: Asymptotic behaviour of throughflow solutions in the class of jeffreys fluids. Continuum Mechanics and Thermodynamics **37**(3) (2025). https://doi.org/10.1007/s00161-025-01384-x
3. Badday, A.J., Harfash, A.J.: Instability in poiseuille flow in a porous medium with slip boundary conditions and uniform vertical throughflow effects. Journal of Engineering Mathematics **135**(1) (2022). https://doi.org/10.1007/s10665-022-10231-w
4. Badday, A.J., Harfash, A.J.: Magnetohydrodynamic instability of fluid flow in a porous channel with slip boundary conditions. Appl. Math. Comput. **432**, 127363 (2022). https://doi.org/10.1016/j.amc.2022.127363
5. Badday, A.J., Harfash, A.J.: Thermosolutal convection in a Brinkman porous medium with reaction and slip boundary conditions. Journal of Porous Media **25**(1), 15–29 (2022). https://doi.org/10.1615/jpormedia.2021038795
6. Bear, J.: Dynamics of Fluids in Porous Media. Dover Publications, New York (1972)
7. Brinkman, H.C.: A calculation of the viscous force exerted by a flowing fluid on a dense swarm of particles. Applied science Research, Al **1**(1), 27–34 (1949). https://doi.org/10.1007/bf02120313
8. Capone, F., De Luca, R., Gianfrani, J.A.: Convection dynamics in a brinkman bidisperse porous medium under internal heating. Transport in Porous Media **152**(10) (2025). https://doi.org/10.1007/s11242-025-02213-0
9. Capone, F., De Luca, R., Massa, G.: Throughflow effect on bi-disperse convection. Ricerche mat. **73**(S1), 67–84 (2023). https://doi.org/10.1007/s11587-023-00811-y
10. Capone, F., De Luca, R., Massa, G.: The combined effects of rotation and anisotropy on double diffusive bi-disperse convection. Ric. Mat. **73**, 2687–2700 (2024). https://doi.org/10.1007/s11587-022-00752-y
11. Capone, F., Gianfrani, J.A.: On the competition between rotation and variable viscosity in a darcy-brinkman model. Proceedings of the Royal Society A: Mathematical, Physical and Engineering Sciences **481**(2312), 20240805 (2025). https://doi.org/10.1098/rspa.2024.0805
12. Christ, C.L.: Remarks on some recently developed devices for summing fourier series for crystal structure analysis. J. Appl. Phys. **18**(12), 1133–1133 (1947). https://doi.org/10.1063/1.1697595
13. Darcy, H.P.G.: Les fontaines publiques de la ville de Dijon: Exposition et application des principes à suivre et des formules à employer dans les questions de distribution d'eau. Victor Dalmont, Libraire des Corps impériaux des ponts et chaussées et des mines, Paris (1856). Atlas plates (54 leaves) engraved by Dulos
14. Devi, J., Sharma, V., Rana, G.C.: Oscillatory modes on the onset of electrohydrodynamic instability in maxwellian nanofluid saturated anisotropic porous layer. Ricerche mat. **74**(1), 249–270 (2023). https://doi.org/10.1007/s11587-023-00778-w
15. Flayyih, H., Khalaf, S.L.: Stability analysis of fractional sir model related to delay in state and control variables. Basra J. Sci. **39**(2), 204–220 (2021). https://doi.org/10.29072/basjs.202123

16. Forchheimer, P.: Wasserbewegung durch boden. Z. Ver. Dtsch. Ing. **45**, 1781–1788 (1901)
17. Fried, E., Gurtin, M.E.: Tractions, balances, and boundary conditions for nonsimple materials with application to liquid flow at small-length scales. Arch. Rational Mech. Anal. **182**, 513–554 (2006). https://doi.org/10.1007/s00205-006-0015-7. Published 13 May 2006; Issue Date: November 2006
18. Giantesio, G., Girelli, A., Lonati, C., Marzocchi, A., Musesti, A., Straughan, B.: Thermal convection in a higher velocity gradient and higher temperature gradient fluid. J. Math. Fluid Mech. **27**(3) (2025). https://doi.org/10.1007/s00021-025-00950-2
19. Grant, M.A., Bixley, P.F.: Geothermal Reservoir Engineering, 2nd edn. Academic Press, Oxford, UK (2011)
20. Harfash, A.: Three dimensional simulation of radiation induced convection. Appl. Math. Comput. **227**, 92–101 (2014). https://doi.org/10.1016/j.amc.2013.11.007
21. Harfash, A.: Three dimensions simulation for the problem of a layer of non-Boussinesq fluid heated internally with prescribed heat flux on the lower boundary and constant temperature upper surface. Int. J. Eng. Sci. **74**, 91–102 (2014). https://doi.org/10.1016/j.ijengsci.2013.08.011
22. Harfash, A.J.: Nonhomogeneous porosity and thermal diffusivity effects on a double-diffusive convection in anisotropic porous media. International Journal of Nonlinear Sciences and Numerical Simulation **17**(5), 205–220 (2016). https://doi.org/10.1515/ijnsns-2015-0139
23. Harfash, A.J.: Stability analysis for penetrative convection in a fluid layer with throughflow. Int. J. Mod. Phys. C **27**(09), 1650101 (2016). https://doi.org/10.1142/s0129183116501011
24. Harfash, A.J., Challoob, H.A.: Nonhomogeneous porosity and thermal diffusivity effects on stability and instability of double-diffusive convection in a porous medium layer: Brinkman model. Nonlinear Engineering **8**(1), 293–302 (2019). https://doi.org/10.1515/nleng-2018-2001
25. Harfash, A.J., Straughan, B.: Magnetic effect on instability and nonlinear stability in a reacting fluid. Meccanica **47**(8), 1849–1857 (2012). https://doi.org/10.1007/s11012-012-9558-x
26. Horton, C.W., Rogers, F.T.: Convection currents in a porous medium. J. Appl. Phys. **16**(6), 367–370 (1945). https://doi.org/10.1063/1.1707601
27. Incropera, F.P., DeWitt, D.P.: Fundamentals of Heat and Mass Transfer, 6th edn. John Wiley & Sons, New York, NY, USA (2006)
28. Kaviany, M.: Principles of Heat Transfer in Porous Media, 2 edn. Springer New York (2012). https://doi.org/10.1007/978-1-4612-4254-3
29. Khalaf, S.L.: Stability analysis and numerical simulation of fractional cholera model. Basra J. Sci. **40**(2), 274–288 (2022). https://doi.org/10.29072/basjs.20220202
30. Khalaf, S.L., Harfash, A.J.: Hydrodynamic stability of convection in porous medium with chemical reaction effect and generalised boundary conditions. Physica D **483**, 135007 (2025). https://doi.org/10.1016/j.physd.2025.135007
31. Khalaf, S.L., Harfash, A.J.: New mathematical methods for convection stability in bidisperse porous media with solute variations. J. Eng. Math. **151**(1) (2025). https://doi.org/10.1007/s10665-025-10438-7
32. Khalaf, S.L., Harfash, A.J.: New mathematical methods for convection stability in bidisperse porous media with solute variations. Journal of Engineering Mathematics **151**(1) (2025). https://doi.org/10.1007/s10665-025-10438-7
33. Khalaf, S.L., Harfash, A.J.: Thermosolutal convection in dual-porosity media with generalized boundary conditions and magnetic field effect. Heat Transfer **54**(7), 4351–4371 (2025). https://doi.org/10.1002/htj.23415
34. Lapwood, E.R.: Convection of a fluid in a porous medium. Math. Proc. Cambridge Philos. Soc. **44**(4), 508–521 (1948). https://doi.org/10.1017/S030500410002452X. Received 13 January 1948
35. Levenspiel, O.: Chemical Reaction Engineering, 3rd edn. John Wiley & Sons, New York, NY, USA (1998)
36. Musesti, A.: Isotropic linear constitutive relations for nonsimple fluids. Acta Mech. **204**(1–2), 81–88 (2008). https://doi.org/10.1007/s00707-008-0050-6
37. Nield, D.A., Bejan, A.: Convection in Porous Media. Springer New York (2013). https://doi.org/10.1007/978-1-4614-5541-7
38. Penrose, R.: A generalized inverse for matrices. Math. Proc. Cambridge Philos. Soc. **51**(3), 406–413 (1955). https://doi.org/10.1017/s0305004100030401
39. Rees, D.A.: The Darcy-Brinkman model for convection in porous-media composites. Transp. Porous Media **42**(2), 303–319 (2001)

40. Rees, D.A.S., Storesletten, L., Postelnicu, A.: The onset of convection in an inclined anisotropic porous layer with oblique principle axes. Transp. Porous Media **62**(2), 139–156 (2006). https://doi.org/10.1007/s11242-005-0618-8
41. Straughan, B.: The Energy Method, Stability, and Nonlinear Convection. Springer New York (1992). https://doi.org/10.1007/978-1-4757-2194-2
42. Straughan, B.: Global nonlinear stability in porous convection with a thermal non-equilibrium model. Proceedings of the Royal Society A: Mathematical, Physical and Engineering Sciences **462**(2066), 409–418 (2005). https://doi.org/10.1098/rspa.2005.1555
43. Straughan, B.: Stability and Wave Motion in Porous Media. Springer New York (2008). https://doi.org/10.1007/978-0-387-76543-3
44. Straughan, B.: Nonlinear stability for thermal convection in a brinkman porous material with viscous dissipation. Transp. Porous Media **134**(2), 303–314 (2020). https://doi.org/10.1007/s11242-020-01446-5
45. Straughan, B.: Competitive porous double diffusion with korteweg stress. Ric. Mat. **73**(S1), 293–307 (2023). https://doi.org/10.1007/s11587-023-00790-0
46. Whitaker, S.: The Forchheimer equation: A theoretical development. Transp. Porous Media **25**(1), 27–61 (1996). https://doi.org/10.1007/BF00141261
47. Zheng, C., Bennett, G.D.: Applied Contaminant Transport Modeling: Theory and Practice, 2nd edn. John Wiley & Sons, Hoboken, NJ, USA (2002)